High-Bandwidth Isolated Voltage Measurements With Very High Common Mode Rejection Ratio for WBG Power Converters

PASCAL S. NIKLAUS (Student Member, IEEE), **RETO BONETTI, CHRISTOF STÄGER,**
JOHANN W. KOLAR (Fellow, IEEE), **AND DOMINIK BORTIS** (Senior Member, IEEE)

Power Electronic Systems Laboratory, Swiss Federal Institute of Technology, Zurich 8092, Switzerland

CORRESPONDING AUTHOR: PASCAL S. NIKLAUS (e-mail: niklaus@lem.ee.ethz.ch)

Initial results of Section II from this paper were presented in part at the 19th IEEE Workshop on Control and Modeling for Power Electronics (COMPEL), Padova, Italy, June 2018.

ABSTRACT Galvanically isolated voltage measurements are becoming increasingly important for the characterization of converter systems with fast switching Wide-Bandgap (WBG) semiconductors. A very high Common Mode Rejection Ratio (CMRR) > 80dB for frequencies up to several tens of MHz is required to accurately measure, e.g., the high-side gate-source or drain-source voltage in a half-bridge, or voltages on floating potentials as, e.g., found in multi-level converters. Common to all listed measurement scenarios is the fast changing reference potential, which acts as Common Mode (CM) disturbance. This article derives the minimum necessary CMRR at different frequencies to constrain the time-domain measurement error below a certain limit. Thereby, only the switched voltage and the voltage transition rate (dv/dt) of the CM disturbance have to be considered and not the actual converter switching frequency f_{sw}. Afterwards, a galvanically isolated measurement system with a CMRR > 100 dB up to 100 MHz and an analog measurement bandwidth of 130 MHz is presented. Critical design aspects to achieve this performance are investigated. Compared to commercially available isolated voltage probes, the presented *measurement system* does not require any additional equipment like an oscilloscope to perform and visualize measurements, since the data is already digitized/sampled and thus can be transmitted directly to a host device (e.g., computer or monitoring system) with corresponding Graphical User Interface (GUI) software. Experimental verification in frequency- and time-domain confirms that the performance is on par with the best commercially available isolated voltage probes.

INDEX TERMS Gate drivers, Isolation technology, Measurement techniques, Power semiconductor switches, Power system measurements, Voltage measurement.

I. INTRODUCTION

Power electronic converter systems with Wide-Bandgap (WBG) semiconductors are key to achieve ever higher efficiencies and power densities, enabling cost-, volume- and weight-efficient conversion of energy within the electrical and/or between electrical and mechanical domain. The very fast switching transitions (high dv/dt) associated with the use of WBG semiconductors help to minimize the semiconductor losses occurring during hard switching [1], [2]. As shown, e.g., in [3], the fast switching transitions demand a significantly increased measurement Bandwidth (BW) up

to several hundred MHz to measure the signals of interest, e.g., the Drain-Source (DS) and/or Gate-Source (GS) voltages. Therefore, high performance measurement tools are required to accurately characterize and verify correct operation. In addition, certain measurements have to be performed on floating reference potential, e.g., in multilevel/multi-cell converters [4], that is, the reference potential of the voltage to be measured differs from the reference potential of the measurement equipment (e.g., the oscilloscope), which is typically referred to Protective Earth (PE). Furthermore, isolation between different
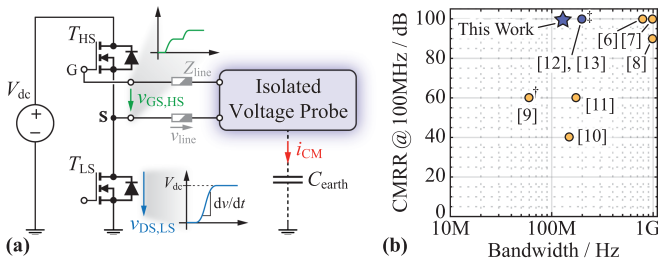
FIGURE 1. (a) High-Side (HS) Gate-Source (GS) voltage ($v_{GS,HS}$) measurement in a half-bridge with a galvanically isolated voltage probe/measurement system. Indicated is the fluctuating/jumping Common Mode (CM) voltage $v_{DS,LS}$ and the parasitic coupling capacitance C_{earth} towards Protective Earth (PE). (b) Different commercially available isolated voltage probes (yellow dots; require an additional, typically vendor-specific oscilloscope) and measurement systems (blue dots; no additional measurement equipment needed) with their reported Bandwidth (BW) and Common Mode Rejection Ratio (CMRR) at 100 MHz. The solution presented in this work is marked with ★. Please note that the probes/systems marked with ‡ and † report the CMRR at only 50 MHz and 60 MHz, respectively.

measurement channels is required when various measurements, all with different reference potential, are performed simultaneously. The scaling of the area-specific on-state resistance with device blocking voltage renders series connection of multiple Low-Voltage (LV) transistors attractive to achieve a certain overall blocking voltage [2]. Thereby, the knowledge of static and/or dynamic device DS voltage sharing, which due to the series connection requires floating low parasitic capacitance measurements, is very important to prevent failures due to overvoltage [5].

From the above listed measurement scenarios, the most critical example is the floating measurement of the High-Side (HS) switch GS voltage $v_{GS,HS}$ between 'G' and 'S,' shown in Fig. 1(a), characterized by a relatively small desired *Differential Mode (DM)* voltage (range of several volts to tens of volts) that is measured referred to a floating reference potential in the range of several hundred volts to kilovolts, which acts as *Common Mode (CM)* voltage. This type of measurement is essential to fully characterize the Gate Driver (GD) circuits and the switching transitions, e.g., to verify the correct dead time, the absence of any cross-conduction (both devices simultaneously on during a short period of time, e.g., due to parasitic turn-on during high dv/dt transitions in combination with low threshold voltage devices), correct current and voltage commutation, overshoot below certain limits and sufficient damping of potential ringing after the switching transitions [3], [14].

In general, the floating measurement reference potential is not steady but fluctuating, i.e., (abruptly) changes its value over time. In the example of the $v_{GS,HS}$ measurement, the fluctuating reference potential (CM voltage) is the DS voltage $v_{DS,LS}$ of the Low-Side (LS) transistor. $v_{DS,LS}$ is referred to PE and transitions between 0 V and V_{dc} with a certain voltage transition rate dv/dt, which in case of WBG semiconductors can easily exceed 100 kV/μs. It is of utmost importance to minimize (or ideally eliminate) the influence of this CM *disturbance* on the measurement. The ability of a floating

measurement system to attenuate/eliminate the impact of unwanted CM disturbances relative to transferring the desired DM measurement signal ($v_{GS,HS}$ in this case) is characterized with the *Common Mode Rejection Ratio (CMRR)*, i.e., the ratio of DM attenuation/gain $\underline{A}_{DM}$ to CM attenuation/gain $\underline{A}_{CM}$, defined as

$$CMRR = \left| \frac{\underline{A}_{DM}}{\underline{A}_{CM}} \right|. \tag{1}$$

Thereby, $\underline{A}_x$ denotes a complex quantity (phasor) with amplitude and phase information and $|\underline{A}_x|$ the absolute value thereof. As will be explained in more detail later, the CMRR typically shows a pronounced frequency dependency, i.e., becomes worse at elevated frequencies above some MHz. In combination with fast CM transients, which generate CM disturbances in the High-Frequency (HF) range, this represents a major challenge for measurement systems.

With the emergence of Insulated-Gate Bipolar Transistors (IGBTs) in the 1990s with comparably faster and larger amplitude switching transitions (multiple kV/μs) compared to back then state-of-the-art Bipolar Junction Transistors (BJTs) and Metal-Oxide-Semiconductor Field-Effect Transistors (MOSFETs), accurate characterization of the GD circuits became ever more important. Thereby, it is necessary to use probes with a high CMRR over a wide frequency range (up to several MHz), as shown, e.g., in [15], where a CMRR of 60 dB at 10 MHz is achieved with an optically isolated measurement system. It will be thoroughly analyzed in this article that the requirements on measurement equipment are much more stringent with today's WBG semiconductor technologies. With a dv/dt of several tens to hundreds of kV/μs, measurement BWs of several hundred MHz and a CMRR of >60 dB above 100 MHz are required [3].

Traditionally, High-Voltage (HV) differential probes are used to perform floating measurements on steady and/or fluctuating reference potential, since they provide a high impedance from both measurement terminals towards PE. A fundamental disadvantage thereby is the equal attenuation of CM and DM signals by a very high ratio (100 to 1000 or even more) and the resulting low Signal-to-Noise Ratio (SNR) and measurement resolution. The desired measurement signal is essentially obtained by subtracting two large voltages, each divided down individually. A further disadvantage of HV differential probes is the typically very poor CMRR at elevated frequencies (above several MHz), limited by the amplitude and phase matching of the differential signal path [16], which inadmissibly deteriorates the measurement in WBG converter systems, e.g., shown in [17]. Different solutions to overcome these limitations have been proposed in literature, e.g., online or offline compensation of the CM influence on the measurement by subtraction of the resulting error in the measurement signal [18] or indirect characterization of the switching transient by integrating the measured switch current [14]. While these methods can help to improve the performance, they are complex to use and do not fully eliminate the measurement error.

Measurements with HV differential probes can be compared to electrical efficiency/loss measurements, where the occurring losses are calculated by subtraction of input and output power. A measurement error of few percent in the individual input and output power measurement can easily lead to errors of $\pm 100\,\%$ in the calculated losses, especially for ultra-high efficiency systems [19]. With a calorimetric measurement setup the occurring losses are directly measured with much higher precision and without information about input and/or output power. In case of floating electrical voltage measurements, a similar measurement setup/system is desired.

In contrast to HV differential probes, the usage of galvanically isolated probes offers inherent isolation of the measurement and decouples the CM and DM signal portions, thus allows to directly measure the DM signal without subtracting large CM signals (which corresponds to calorimetric efficiency measurements where independent from input/output power directly the losses are measured). A single-ended realization is feasible and therefore, the CMRR does not depend on close matching of differential signal paths. Thereby, all limitations of HV differential probes in the presented measurement scenarios are mitigated. Galvanically isolated measurements are widely used in Medium-Voltage (MV) applications and in harsh environments, exposed to high noise, switching surges and interferences [20], demanding for robust measurement systems, e.g., in plasma physics experiments [21], in HV electric substations to quantify the electromagnetic compatibility [22] or to assess the quality of the power distribution grid [23]. An optical link (analog or digital) is mostly used as isolated transmission channel [20], [21], [23] but also wireless communication channels have been investigated [24], [25].

The trend of ever higher required CMRR at elevated frequencies has been recognized by different test and measurement equipment manufacturers and there is a variety of isolated probes/measurement systems commercially available that achieve these requirements. The most important of which are shown in Fig. 1(b), plotted in a plane of their measurement BW and achieved CMRR at 100 MHz. The yellow dots [6], [7], [8], [9], [10], [11] thereby denote *isolated voltage probes*, which require an additional, often vendor-specific (except [11]) oscilloscope to perform measurements, whereas the blue dots [12], [13] designate *isolated measurement systems*, which only require a host computer with respective Graphical User Interface (GUI) software to display the measurements. This important difference between a measurement probe and a measurement system has to be kept in mind when evaluating possible solutions from various points of view such as flexibility, ease of use and cost. Please note that [12] and [13] have a BW of 200 MHz but specify the CMRR only up to 50 MHz (marked with ‡ in Fig. 1(b)), which means that at 100 MHz, approximately 10 dB less can be expected. Similarly, [9] has a BW of only 60 MHz and the indicated CMRR value is valid at 60 MHz (marked with † in Fig. 1(b)).

The devices listed in Fig. 1(b) all show a very high CMRR and BW performance. An important question is therefore, how much CMRR at which frequency is really required to successfully perform the desired measurements, i.e., which of the listed devices suit the task. With help of the analyses carried out in Section II, the minimum required CMRR at different frequencies is derived to limit the time-domain measurement error below a certain threshold. It is shown that the required CMRR reduces above a frequency defined solely by the voltage transition time. Even though isolated probes/measurement systems are fully isolated from PE, their CMRR also degrades at higher frequencies. The origin of this effect is thoroughly explained and in combination with the discussion of different key aspects to design an isolated measurement system with superior HF CMRR, a possible realization is presented in Section III. In contrast to commercially available *probes*, the presented *system* is independent of any specific oscilloscope and can directly be used to perform measurements. Influences of different external factors such as connection to Devices Under Test (DUTs) and the usage of an auxiliary isolated Power Supply Unit (PSU) are experimentally investigated and the performance of the presented system is verified and compared with the best currently available commercial isolated probe in Section IV. Finally, Section V concludes the article.

II. DERIVATION OF CMRR REQUIREMENTS
This section extends initial analyses from [16].

A. MODELING OF DISTURBANCE AND MEASUREMENT ERROR
In power electronic converter systems, the modeling of the CM excitation is typically simplified and given by a trapezoidal switched voltage v_{sw}, e.g., the DS voltage $v_{DS,LS}$ of the LS switch in a half-bridge (cf. Fig. 1(a)). Thereby, a constant voltage transition rate dv/dt is assumed, mainly determined by the utilized semiconductor technology, e.g., $100\,\text{kV}/\mu\text{s}$ for Gallium Nitride (GaN). The transition time t_s then results from the amplitude V_{dc} of the switched voltage v_{sw}.

Fig. 2(a) shows the trapezoidal CM switch-node voltage $v_{sw}(t)$ with pulse width t_p and switching frequency $f_{sw} = 1/T_{sw}$, transitioning between $0\,\text{V}$ and V_{dc} (and vice versa) with a transition time $t_s = \frac{V_{dc}}{dv/dt}$. Its spectral representation with the spectral components $\underline{\hat{V}}_{sw}(n \cdot f_{sw})$ is shown in Fig. 2(c) for two cases with equal V_{dc}, t_p and t_s but two different switching frequencies $f_{sw,I}$ (case I, blue) and $f_{sw,II} = 10 \cdot f_{sw,I}$ (case II, orange). The spectral envelope (dashed lines) of this *disturbance voltage* has two corner frequencies f_{c1} and f_{c2}, defined as [26]

$$f_{c1} = \frac{1}{\pi \cdot t_p} = \frac{f_{sw}}{\pi \cdot D} \tag{2}$$

$$f_{c2} = \frac{1}{\pi \cdot t_s} = \frac{dv/dt}{\pi \cdot V_{dc}} \tag{3}$$
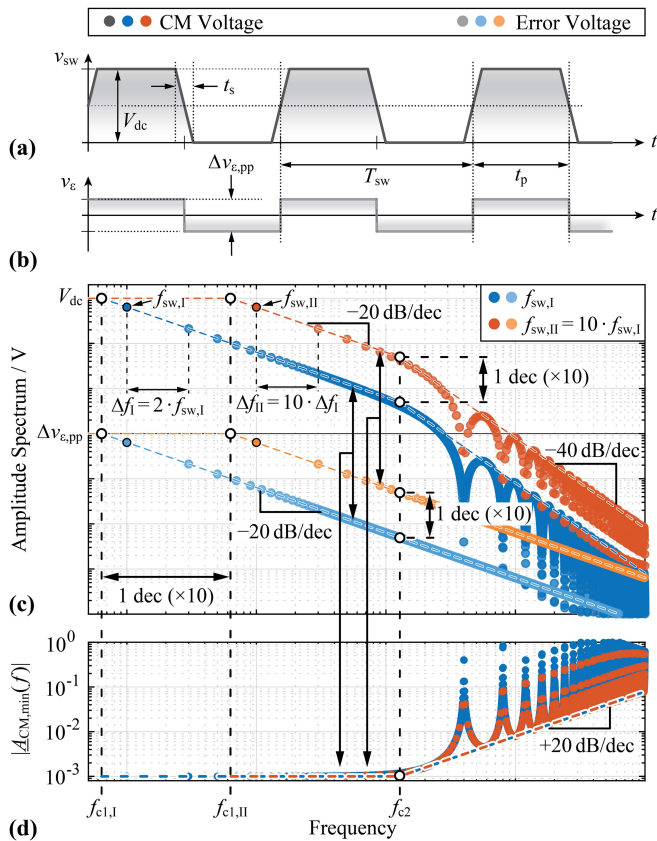
FIGURE 2. Exemplary time-domain view of (a) the trapezoidal CM voltage (switch-node voltage) v_{sw} with pulse width t_P, occurring at switching frequency $f_{sw} = 1/T_{sw}$ with rise/fall times t_s and (b) the resulting worst-case square-shaped error voltage v_ε with peak-to-peak value $\Delta v_{\varepsilon,pp}$. (c) Frequency-domain representation of v_{sw} and v_e for two switching frequencies, $f_{sw,II} = 10 \cdot f_{sw,I}$ with indicated corner frequencies $f_{c1,I}$, $f_{c1,II}$ and f_{c2}. (d) Resulting minimum required CM attenuation to limit the time-domain error below a certain peak-to-peak limit $\Delta v_{\varepsilon,pp}$ (1/1000 of V_{dc} in this exemplary case).

with the duty-cycle $D = t_p/T_{sw}$. The spectral envelope can be divided in three regions:

i) Constant value of V_{dc} for $f < f_{c1}$,
ii) Decay with $-20\,\mathrm{dB/dec}$ for $f_{c1} \leq f < f_{c2}$,
iii) Decay with $-40\,\mathrm{dB/dec}$ for $f \geq f_{c2}$.

In a practical measurement situation, the maximum tolerable peak-to-peak voltage error $\Delta v_{\varepsilon,pp}$ of the actual DM measurement is typically quantified in time-domain and depends on the application. In the exemplary case of the $v_{GS,HS}$ measurement, the voltage measurement range can be between several volts (e.g., ranging from $-6\,\mathrm{V}$ to $+6\,\mathrm{V}$ for GaN switches) up to several tens of volts (e.g., $-5\,\mathrm{V}$ to $+20\,\mathrm{V}$ for Silicon-Carbide (SiC) switches). Assuming, for example, a full-scale DM measurement range of 25 V and a desired accuracy of 1 %, $\Delta v_{\varepsilon,pp}$ must be below 250 mV. The worst-case *error voltage* $v_\varepsilon(t)$ that fulfills $(\max\{v_\varepsilon(t)\} - \min\{v_\varepsilon(t)\}) \leq \Delta v_{\varepsilon,pp}$ is a square-shaped voltage with pulse width t_p, period T_{sw} and peak-to-peak value $\Delta v_{\varepsilon,pp}$, i.e., the measured voltage always deviates $\pm \Delta v_{\varepsilon,pp}/2$ (e.g., $\pm 125\,\mathrm{mV}$) from

the real signal. Generally, this is assumed to be much worse than having the measured voltage disturbed just during the voltage transitions. This worst-case error voltage is shown in Fig. 2(b) (time-domain) and Fig. 2(c) (frequency-domain; again for two switching frequencies $f_{sw,I}$ in light blue and $f_{sw,II} = 10 \cdot f_{sw,I}$ in light orange) with spectral components $\hat{V}_\varepsilon(n \cdot f_{sw})$. The spectral envelope is in this case composed of only two regions:

i) Constant value of $\Delta v_{\varepsilon,pp}$ for $f < f_{c1}$,
ii) Decay with $-20\,\mathrm{dB/dec}$ for $f \geq f_{c1}$.

The required CM attenuation of a measurement system/probe can be thought of as a filter with Transfer Function (TF) $\underline{A}_{CM}(f)$, which attenuates the CM disturbance voltage v_{sw} to the error voltage v_ε [15]. Each spectral component $\hat{V}_\varepsilon(n \cdot f_{sw})$ of v_ε can be written as

$$\hat{\underline{V}}_\varepsilon(n \cdot f_{sw}) = \underline{A}_{CM}(f) \cdot \hat{\underline{V}}_{sw}(n \cdot f_{sw}) \tag{4}$$

where n is the harmonic order ($n \in \mathbb{N}$). Here, it is assumed that $\underline{A}_{CM}$ has no phase-shift, i.e., the components $\hat{\underline{V}}_{sw}(n \cdot f_{sw})$ are scaled only in amplitude ($A_{CM} = |\underline{A}_{CM}|$). From the spectral envelopes of v_{sw} and v_ε, the minimum required CM attenuation $|\underline{A}_{CM,min}(f)|$ shown in Fig. 2(d) can be graphically determined and it shows for both exemplary disturbance signals of Fig. 2(a) equally a constant value $A_{CM,min,0} = \Delta v_{\varepsilon,pp}/V_{dc}$ for $f < f_{c2}$ and rises with $+20\,\mathrm{dB/dec}$ for $f \geq f_{c2}$. This leads to the very important conclusion that *the minimum required CM attenuation is independent of the converter switching frequency f_{sw} and depends only f_{c2}*, i.e., on the amplitude V_{dc} of the switch-node voltage v_{sw} and the voltage transition rates dv/dt (cf. (3)).

The spectrum of v_{sw} of case I compared to case II starts to decay one decade earlier ($f_{sw,I} = f_{sw,II}/10$). Hence, for $f \geq f_{sw,II}$ the spectral envelope of case I is by a factor 10 lower than the envelope of case II, which could lead to the assumption that $|\underline{A}_{CM,min}(f)|$ in case I compared to case II is correspondingly lower by a factor of 10. This is, however, not true because in case I, also the envelope of the maximum allowed v_ε starts to decay one decade earlier and therefore, the ratio between $|\hat{\underline{V}}_\varepsilon|$ and $|\hat{\underline{V}}_{sw}|$ is the same for each occurring frequency component in both cases. An intuitive explanation is that the maximum level of distortion caused by a switching transition is independent of how often this transition repeats. An alternative way of looking at this is that in case I the spectral components of $\hat{\underline{V}}_{sw}(n \cdot f_{sw})$ and $\hat{\underline{V}}_\varepsilon(n \cdot f_{sw})$ are indeed ten times lower than in case II but at the same time also ten times denser, i.e., $\Delta f_I = 2 \cdot f_{sw,I} = \Delta f_{II}/10$ [16]. Thus, the signal *energy* (related to the Root Mean Square (RMS) value) is the same in both cases, which intuitively explains that $|\underline{A}_{CM,min}|$ has to be identical in both cases.

B. PRACTICAL CASES AND REQUIRED CMRR

Knowing the operating voltage V_{dc} and the voltage transition rates dv/dt, the minimum required CM attenuation $|\underline{A}_{CM,min}(f)|$ can directly be determined for a given maximum tolerable peak-to-peak time-domain measurement error $\Delta v_{\varepsilon,pp}$ and therefore, a suitable measurement probe/system
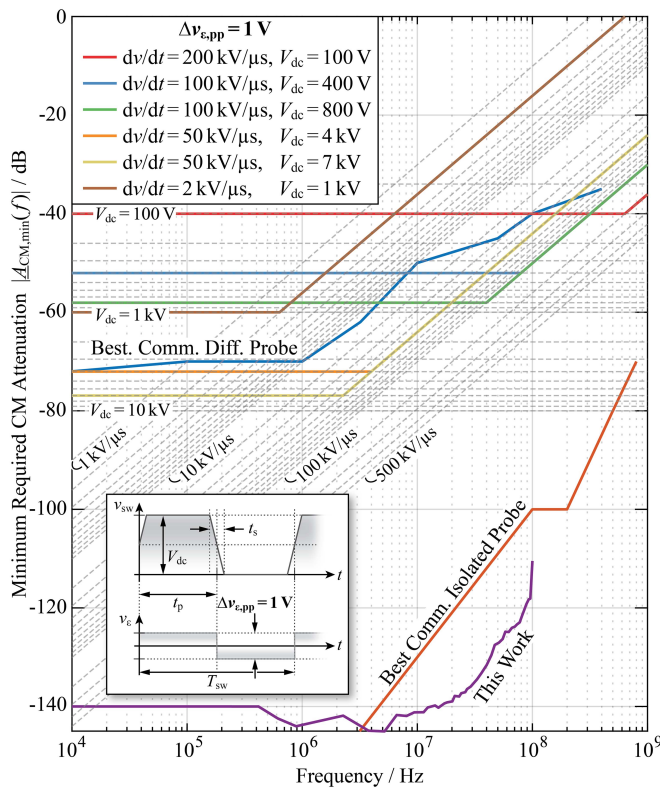
FIGURE 3. Minimum required CM attenuation based on Fig. 2 to constrain $\Delta v_{\varepsilon,\mathrm{pp}}$ to 1 V peak-to-peak for different values of the dc link voltage V_{dc} and different switching transition rates $\mathrm{d}v/\mathrm{d}t$. Some typical combinations of V_{dc} and $\mathrm{d}v/\mathrm{d}t$ are highlighted with colors. For a lower/higher allowed $\Delta v_{\varepsilon,\mathrm{pp}}$ the plot can simply be shifted down/up along the y-axis (e.g., for 100 mV, 20 dB more CM attenuation is required). Further indicated are the CMRR frequency responses for the best-performing commercially available high-voltage differential probe (blue) and optically isolated probe (orange) together with the achieved CMRR of this work (purple).

can be selected. Datasheets typically specify the frequency response of the CMRR referred to the input, i.e., any attenuation and/or amplification in the DM signal path is already corrected. This means, $\underline{A}_{\mathrm{DM}}$ in (1) is unity and the minimum required CMRR directly corresponds to the inverse of $|\underline{A}_{\mathrm{CM,min}}|$.

Fig. 3 shows the minimum required CM attenuation $|\underline{A}_{\mathrm{CM,min}}(f)| = 1/\mathrm{CMRR}_{\mathrm{min}}(f)$ (expressed in dB, i.e., $\mathrm{CMRR}_{\mathrm{min,dB}} = -A_{\mathrm{CM,min,dB}}$) for different values of V_{dc} and $\mathrm{d}v/\mathrm{d}t$ that leads to $\Delta v_{\varepsilon,\mathrm{pp}} = 1$ V. For lower/higher admissible $\Delta v_{\varepsilon,\mathrm{pp}}$, $|\underline{A}_{\mathrm{CM,min}}|$ is simply shifted down/up. A reduction/increase of $\Delta v_{\varepsilon,\mathrm{pp}}$ by a factor of ten, for example, leads to a $-20\,\mathrm{dB}/+20\,\mathrm{dB}$ shift of $|\underline{A}_{\mathrm{CM,min}}|$. Some combinations of V_{dc} and $\mathrm{d}v/\mathrm{d}t$ typically found in practical converter realizations are highlighted with different colors in Fig. 3. For example, a converter with GaN semiconductors with a $\mathrm{d}v/\mathrm{d}t = 100\,\mathrm{kV/\mu s}$ and a dc link voltage $V_{\mathrm{dc}} = 800\,\mathrm{V}$, $|\underline{A}_{\mathrm{CM}}| < -70\,\mathrm{dB}$ (CMRR > 70 dB) at 100 MHz is required to constrain the time-domain measurement error below 100 mV (green line shifted down by 20 dB). Furthermore, the datasheet values for the best-performing commercially available HV differential probe (blue) and optically isolated
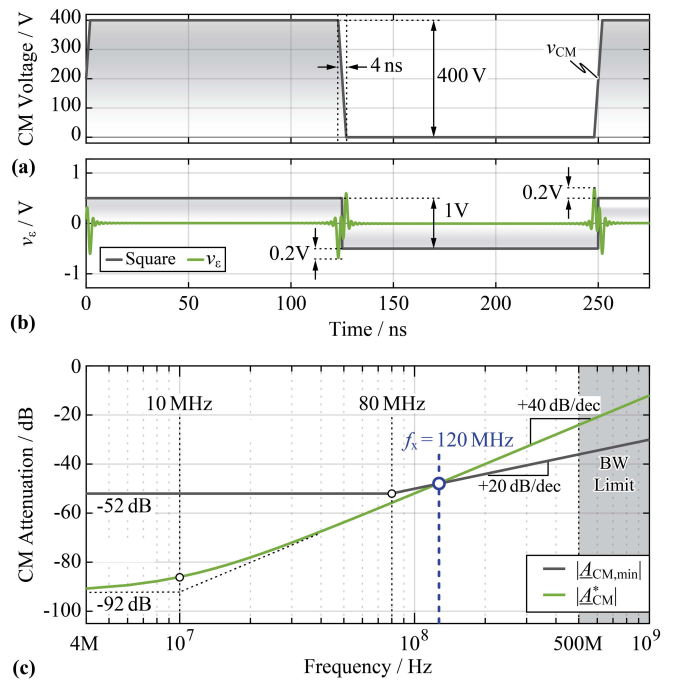

FIGURE 4. (a) Exemplary CM disturbance with $V_{\mathrm{dc}} = 400$ V and $\mathrm{d}v/\mathrm{d}t = 100\,\mathrm{kV/\mu s}$. (b) Time-domain measurement error voltage v_{ε} resulting from a violation of the minimum required CM attenuation, which would result in the square-shaped error voltage (gray). (c) Exemplary CM attenuation frequency response that leads to v_{ε} in (b) (green), rising with $+40\,\mathrm{dB/dec}$ after a certain corner frequency to more realistically represent the behavior of a galvanically isolated probe/measurement system.

probe (orange) as well as the solution presented in this article (purple) are indicated (up to their respective measurement BW). Fig. 3 clearly shows that HV differential probes are insufficient for measurements on fluctuating reference potential in WBG converters with high $\mathrm{d}v/\mathrm{d}t$ above several tens of kV/µs, even for a relatively large allowed error voltage of 1 V peak-to-peak. They are, however, sufficient in applications with lower switching transition rates, e.g., in IGBT converters with $V_{\mathrm{dc}} = 1\,\mathrm{kV}$ and $\mathrm{d}v/\mathrm{d}t = 2\,\mathrm{kV/\mu s}$ (brown curve in Fig. 3).

It has to be noted that Fig. 3 indicates the absolute minimum required $|\underline{A}_{\mathrm{CM}}|$ in order to achieve the said square-shaped error voltage. In practice, galvanically isolated voltage probes achieve quasi-infinite CMRR at low frequencies, which means that the Low-Frequency (LF) components are much stronger attenuated and only error pulses around the transitions of v_{sw} remain (cf. green curves in Fig. 4).

C. REASONS FOR DECREASING CMRR AT ELEVATED FREQUENCIES

A certain geometry-dependent parasitic capacitance C_{earth} is inherently formed between any galvanically isolated probe/measurement system and the steady reference potential, usually PE. Typical values are in the range of 5–20 pF. A CM excitation with a certain $\mathrm{d}v_{\mathrm{sw}}/\mathrm{d}t$ results in a CM

current/charging current

$$i_{\mathrm{CM}} = C_{\mathrm{earth}} \cdot \frac{\mathrm{d}v_{\mathrm{sw}}}{\mathrm{d}t}, \tag{5}$$

which for exemplary values of $C_{\mathrm{earth}} = 10\,\mathrm{pF}$ and $\mathrm{d}v_{\mathrm{sw}}/\mathrm{d}t = 100\,\mathrm{kV/\mu s}$ equals $1\,\mathrm{A}$. This current has to flow through the connection between Device Under Test (DUT) and probe and thereby deteriorates the measurement, e.g., by generating a voltage drop v_{line} across the typically ohmic-inductive connection impedance Z_{line} (cf. Fig. 1(a)), which without further measures translates into a measurement error. Thus, i_{CM} ultimately defines the CMRR.

Representing (5) in the frequency-domain means that i_{CM} increases linearly with frequency (capacitive impedance of C_{earth} is inversely proportional to f), i.e., with $+20\,\mathrm{dB/dec}$. In combination with the said ohmic-inductive impedance Z_{line} of the connection between DUT and probe (indicated in Fig. 1(a)), which due to its inductive part increases with $+20\,\mathrm{dB/dec}$, the voltage drop v_{line} across this connection rises with $+40\,\mathrm{dB/dec}$. Therefore, $|\underline{A}_{\mathrm{CM}}(f)|$ of isolated measurement systems typically increases with $+40\,\mathrm{dB/dec}$ (equivalently, the CMRR decreases with $-40\,\mathrm{dB/dec}$), corresponding to a second-order system. Because the minimum required CM attenuation $|\underline{A}_{\mathrm{CM,min}}|$ rises with $+20\,\mathrm{dB/dec}$ but the actual $|\underline{A}_{\mathrm{CM}}|$ of real isolated measurement systems rises with $+40\,\mathrm{dB/dec}$, there exists a certain intersection frequency f_{x}, above which $|\underline{A}_{\mathrm{CM}}|$ is above $|\underline{A}_{\mathrm{CM,min}}|$. This is exemplary shown in Fig. 4 for a CM disturbance with $V_{\mathrm{dc}} = 400\,\mathrm{V}$, a $\mathrm{d}v/\mathrm{d}t = 100\,\mathrm{kV/\mu s}$ and a maximum allowed $\Delta v_{\varepsilon,\mathrm{pp}} = 1\,\mathrm{V}$. The square-shaped error signal in Fig. 4(b) is achieved with the minimum required CM attenuation $|\underline{A}_{\mathrm{CM,min}}| = -52\,\mathrm{dB}$ up to $80\,\mathrm{MHz}$, then rising with $+20\,\mathrm{dB/dec}$, depicted with the gray curve in Fig. 4(c). Further depicted is an arbitrarily selected CM attenuation frequency response $|\underline{A}_{\mathrm{CM}}^{*}|$ with a dc value of $-92\,\mathrm{dB}$ ($40\,\mathrm{dB}$ better than required) and a $+40\,\mathrm{dB/dec}$ increase starting at $f = 10\,\mathrm{MHz}$, which more accurately represents the behavior of real isolated probes/measurement systems. The intersection of the two attenuation curves is at $f_{\mathrm{x}} = 120\,\mathrm{MHz}$. This means that spectral components below/above f_{x} are stronger/weaker attenuated than required, which leads to a reduction (or quasi elimination) of the steady-state value in the square-shaped time-domain error voltage but due to the weaker attenuated HF components to an increase of $\approx 0.2\,\mathrm{V}$ during the CM voltage transitions, as indicated in Fig. 4(b). Therefore, in real isolated measurement systems, the time-domain error voltage v_{ε} due to a CM disturbance is composed of HF pulses/oscillations around the transitions of the CM voltage. If f_{x} lies above the desired measurement BW f_{BW} (indicated with a BW limit of $500\,\mathrm{MHz}$ in Fig. 4(c)), there would be no increase of the HF components, since everything above f_{BW} would anyway be attenuated by a filter, i.e., a too low CMRR in this frequency range is not a concern.

III. PRACTICAL REALIZATION OF A GALVANICALLY ISOLATED VOLTAGE MEASUREMENT SYSTEM
A. OPERATING PRINCIPLE OF EXISTING SOLUTIONS
Having defined the required CMRR at different frequencies, this section presents a possible realization of a galvanically isolated measurement system, which in contrast to an isolated probe does not need a connection to an oscilloscope but allows to visualize and evaluate measurements directly on a host device (computer, laptop, tablet, etc.) with corresponding GUI software. Besides maximum flexibility, this is advantageous regarding total measurement equipment cost, since no oscilloscope (often vendor-specific) has to be utilized. To the author's knowledge, all commercially available isolated measurement probes and systems are realized either with a real-time analog ([6], [7], [8], [9], [10], [11]) or digital ([12], [13]) optical link with a transmitter (probe head) and a receiver (part connected to the oscilloscope, usually referred to PE). Comprehensive experimental investigation has shown that any system that converts the measured signal back into the analog domain, e.g., to connect to an oscilloscope, is prone to distortions that couple into the typically PE-referred receiver side. This can be mitigated with very careful placement (long distance of ideally several meters between the probe transmitter and its receiving unit) and extensive shielding of the probe, its receiver and the oscilloscope. Only with such a *Golden Setup*, clearly unsuitable in everyday laboratory applications, it is possible to even measure/verify the indicated CMRR of $> 100\,\mathrm{dB}$ at $f > 100\,\mathrm{MHz}$ of some commercial probes (cf. Fig. 1(b)).

As alternative realization option it is therefore advisable to directly digitize the measurement signal with an Analog-to-Digital Converter (ADC) as close as possible to the measurement point and process/visualize the data solely in digital form in order to be less sensitive to distortions (in the analog domain, every millivolt of distortion directly impairs the measurement, whereas in the digital domain, the distortion must be several volts to cause one or multiple bits to flip and thus, to distort the measurement). The digitized data is then transmitted via an isolated channel to a host unit for visualization and processing. This can be done either in real-time or only the relevant subset of the acquired data (e.g., after a specified trigger condition) can be transmitted over a narrow-band wireless transmission channel, e.g., Bluetooth, with much lower throughput compared to a real-time link [24]. With a sampling rate of 500 Megasamples Per Second (MSPS) and a vertical resolution of $8\,\mathrm{Bit}$, a real-time transmission channel would need a minimum throughput of $4\,\mathrm{GBit/s}$ (without any encoding scheme). Besides the more complex realization on the transmitter side and the relatively high power consumption of such high-throughput channels, additional hardware on the receiver side would be required as interface to a host device. A direct interface to the digital signal processing unit in standard oscilloscopes to directly visualize and synchronize the captured data from the isolated system together with other measurements would be a promising solution. Unfortunately,
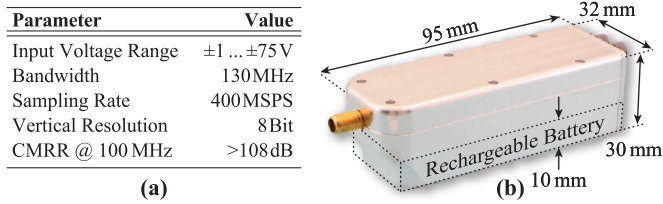
Parameter	Value
Input Voltage Range	±1 ... ±75 V
Bandwidth	130 MHz
Sampling Rate	400 MSPS
Vertical Resolution	8 Bit
CMRR @ 100 MHz	>108 dB

(a)

(b)

FIGURE 5. (a) Specifications and (b) picture of the presented high BW isolated measurement system with superior HF CMRR, including the overall dimensions (incl. shielding enclosure + rechargeable battery).

FIGURE 6. (a) Schematic overview of the single-ended galvanically isolated voltage measurement system. The relevant parts to achieve superior CMRR at high frequencies are highlighted in blue. (b) Layout representation of the system with important parts highlighted and labeled. (c) Picture of the 16 cm long triaxial tip cable equipped with cable CM cores (cable CMC).

such a port is not provided on most oscilloscopes. Therefore, the *WiScope*, a battery-powered isolated oscilloscope presented in [25], uses a Bluetooth wireless data channel to connect to a host device. Thanks to the Bluetooth interface, basically any device with corresponding GUI software (computer, laptop, tablet, etc.) can act as host. It achieves an analog BW of 100 MHz and a CMRR of 100 dB up to roughly 5–6 MHz, which is suitable for slow switching transitions, e.g., found in power converters featuring IGBTs. At 100 MHz, however, the CMRR reduces to ≈50 dB, which according to previously conducted analyses of Section II is not enough for measurements with WBG converters (cf. Fig. 3).

B. IMPROVED MEASUREMENT SYSTEM

The numerous advantages regarding handling and flexibility offered by the WiScope motivate to use it as basis for the design of an improved isolated measurement system with significantly higher HF CMRR, mainly achieved with a carefully designed and very compact Analog Front-End (AFE) and with a sophisticated connection between the measurement point of the DUT and the AFE. The system specifications are listed in Fig. 5(a) and Fig. 5(b) shows a picture of the finalized prototype and its dimensions (further indicated is the volume occupied by the rechargeable battery accounting for approximately 1/3 of the total volume). While the BW, input voltage range, sampling rate and vertical resolution are identical to the WiScope, a CMRR of more than 100 dB at 100 MHz is achieved (improvement by several orders of magnitude).

Fig. 6(a) shows a simplified circuit of the galvanically isolated voltage measurement system and Fig. 6(b) the top-side view of the Printed Circuit Board (PCB) with the relevant building blocks highlighted. The measurement system is connected to a DUT (e.g., a half-bridge as shown in Fig. 1(a)) with a coaxial connection cable (hereinafter denoted tip cable). A picture of the tip cable equipped with CM cores is depicted in Fig. 6(c) (details follow below). The DM signal path is composed of a single-ended, frequency compensated input voltage divider (1:50 division ratio with $R_1C_1 = R_2C_2$, $R_1 = 910 \text{ kOhm}$ and $C_1 = 1 \text{ pF}$), followed by a high-impedance unity-gain buffer (Analog Devices ADA4817) acting as impedance transformer. The gain is adjusted with a Variable Gain Amplifier (VGA) (Texas Instruments LMH6574) and the signal is low-pass filtered with an Anti Aliasing Filter (AAF) (5th order Butterworth filter with
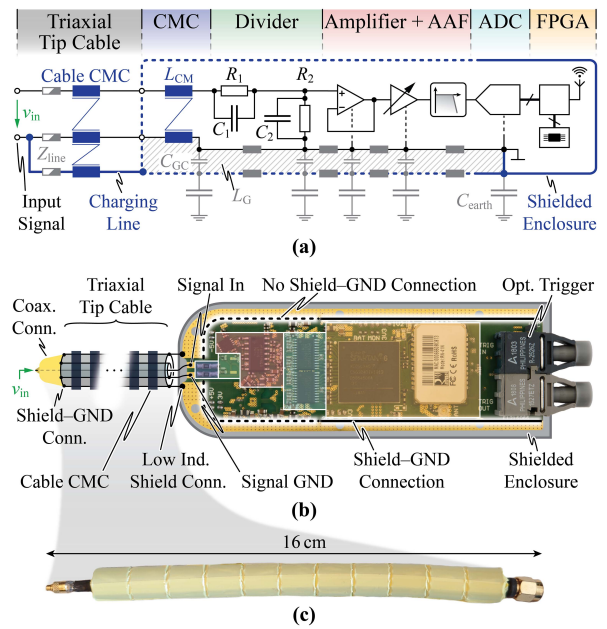
corner frequency $f_{\text{AAF}} \approx 130 \text{ MHz}$) before it is digitized by an ADC with a sampling rate of 400 MSPS and a vertical resolution of 8 Bit (two interleaved Texas Instruments ADC08200 with 200 MSPS each). To maximize the conversion resolution for various desired full-scale input voltage ranges, the AFE overall gain is configurable with the VGA and with adjustable voltage references for the ADC. Overall, the full-scale input voltage range can be adjusted between ±0.8 V and ±50 V. A Field-Programmable Gate Array (FPGA) is the interface to a 100 kilosamples ring buffer (memory) that continuously stores the incoming sampled measurement points until at a specific trigger condition (configured on the host GUI software) the acquisition is stopped and the content of the memory is sent to the host via the Bluetooth wireless data link. With the maximum sampling rate of 400 MSPS, measurements up to 250 μs duration can be stored. Longer measurement records can be stored with a reduced sampling rate of the ADC.

Recalling from above, the only limiting factor for the (HF) CMRR in an isolated voltage probe/measurement system is the charging current i_{CM} of C_{earth} (cf. (5)), leading to erroneous voltage drops across any parasitic (typically ohmic-inductive) impedances along its path (tip cable impedance Z_{line} indicated in Fig. 6(a) or ground loop inductance on the PCB). Therefore, there are two obvious measures to improve the CMRR, i.e., minimize i_{CM}:

i) C_{earth} has to be as small as possible – according to $C_{\text{earth}} \propto A/d$, this is achieved with a very compact overall system (small surface A) and by placing the system with a certain distance d away from PE.

ii) C_{earth} has to be decoupled from the fast CM voltage transition, i.e., a certain CM impedance (e.g., Common Mode Chokes (CMCs)) must be inserted between the CM disturbance and C_{earth}.

However, i_{CM} cannot be vanished completely, hence further measures (highlighted in dark blue in Fig. 6(a)) ensure that it flows separated from the small DM current that builds the voltage across R_2 and C_2 (desired measurement signal), and therefore, does not alter the measurement:

i) Lossy ferrite suppression cores (CM cores) placed on the tip cable form a single-turn cable CMC that provides a high CM impedance to decouple C_{earth} from the fast voltage transients (switch-node of the half-bridge), as proposed in [27], [28]. Multiple cores stacked on the full length of the cable minimize the parasitic capacitance, i.e., ensure maximum CM impedance up to HF. For fast CM transients (f_{c2} above the resonance frequency $f_{0,line}$ formed by the inductive part of Z_{line} and C_{earth}, typically in the range of a few tens to hundreds of MHz), the full CM voltage initially appears across the tip cable (and thereby across the CM cores), which could saturate the cores and vanish the CM impedance. A higher number of cores maximizes the core cross-section area and helps to minimize the risk of saturation for a given voltage. Simulation with the utilized tip cable (16 cm long and with 11 cores of type 2643480102 from Fair-Rite, depicted in Fig. 6(c)), an assumed $C_{earth} = 10\,pF$ and a CM excitation with 10 kV reveals a worst-case peak flux-density $< 100\,mT$, which is sufficiently below the saturation flux density of the magnetic material. The occurring peak flux density is independent of the repetition rate, i.e., switching frequency, of the CM excitation. A further benefit of the CM cores is the damping of the aforementioned resonance between Z_{line} and C_{earth} by the resistive component of the resulting CM cable impedance, which otherwise could cause significant peaking in the CMRR. Note that instead of ferrite materials, the cores could also be made of nanocrystalline materials such as, e.g., Vitroperm 500F from Vacuumschmelze. The latter offer a significantly higher dc permeability ($\approx40'000$) compared to ferrites and also give enough resistive contribution at HF to damp occurring resonances. At HF ($>10\,MHz$), however, they show a very similar permeability to the utilized ferrite cores (both a few hundred to 1000). A benefit, however, is the higher saturation flux density (1–2 T compared to several 100 mT), which, however, in this case is not strictly required as shown above (peak flux-density $<100\,mT$). Moreover, nanocrystalline cores are considerably more expensive than ferrites due to the more complex manufacturing process.

ii) The decoupling of C_{earth} from the CM source by means of the tip cable CM impedance from i) is not perfect, hence, there is still a certain i_{CM} flowing. To let this current flow independent of the DM measurement current,

instead of just two connection lines between DUT and measurement system, one high-impedance signal line and one ground line, the proposed system uses a *three-wire* tip cable in triaxial configuration (cf. Fig. 6(b) on the left side and picture in Fig. 6(c)). The center wire is the high-impedance signal line and the two outer conductors are connected together at the DUT side (labeled with 'Shield-GND Conn.' in Fig. 6(b)) but are separately connected to the measurement system. The middle connector is the low-impedance ground line (return path for the small measurement signal DM current) whereas the outer connector acts as a separate *charging line* that carries ideally the full i_{CM} and is connected directly to a metallic enclosure with as low an impedance as possible (labeled 'Low Ind. Shield Conn.' in Fig. 6(b)). This enclosure effectively shields the sensitive measurement circuit on the PCB by defining C_{earth} with its outer surface and realizing an equipotential, ideally distortion-free zone inside. The finalized measurement system in Fig. 5(b) has a C_{earth} of approximately 7 pF (including tip cable) when placed in a defined environment (metallic box connected to PE) at a distance of $\approx15\,cm$ to each side on a non-conductive distance holder (cf. Section IV-A).

iii) Theoretically, C_{earth} would be charged solely via the charging line according to ii) and no CM current would flow through the signal and ground lines. In practice, this is unfortunately not the case due to nonzero impedance of the charging line. To prevent CM current flow in the signal and ground lines, an additional CM choke L_{CM} (TDK Corporation ACM2510-102) is placed in these two lines, which takes the residual CM voltage appearing across the nonzero impedance of the charging line. Clearly, L_{CM} must provide maximum CM impedance but at the same time must be realized as compact as possible, in order to keep the overall size of the distortion-sensitive AFE small. Moreover, it must feature very high coupling as otherwise the residual DM inductance (leakage inductance) causes inadmissibly high peaking in the DM frequency response due to resonance with the tip cable capacitance and inductance as well as the AFE input capacitance. Due to the compact layout, the circuit ground on the PCB and the shield are capacitively coupled (indicated in Fig. 6(a)), which for HF prevents saturation of L_{CM}. To avoid significant fluctuations between the circuit ground and the shield potential, which particularly at LF could lead to a saturation of L_{CM}, the circuit ground is connected to the shielding enclosure *after* the ADC (labeled 'Shield-GND Connection' in Fig. 6(b)). A connection after the ADC is less critical, because there, all signals are digital and less sensitive to small voltage errors (voltage drops across PCB tracks) in case a small CM current would flow on this part of the PCB. The loop inductance L_G between ground and shield (indicated in Fig. 6(a)), formed by the physical layout, in

addition to L_{CM} helps to drive i_{CM} solely through the charging line.

The very compact AFE depicted in Fig. 6(a) is possible thanks to the single-ended realization and is a general advantage to minimize the overall system size and thereby C_{earth}. Furthermore, since it is the most critical part due to its high distortion-susceptibility, the short signal and ground return paths between the analog input and the ADC help to minimize parasitic voltage drops due to residual CM currents. In contrast to the single-ended realization of the AFE depicted in Fig. 6(a), a fully differential variant would also be possible. Two high-impedance signal lines (positive and negative), each connected to an input voltage divider, would lead to i_{CM} almost entirely flowing though the low-impedance charging line (current divider). The fully-differential approach could potentially further improve the CMRR, since any residual voltage drops along the circuit ground act as CM to the subsequent differential amplifier and compared to the single-ended approach do not directly deteriorate the DM measurements. The downside is, however, the requirement of precise matching between the differential signal paths (similar to HV differential probes) [29] and increased complexity and size of the AFE. With full integration of the AFE circuit into one single chip, the matching as well as the circuit size could be significantly optimized. As will be seen in Section IV, however, the single-ended approach presented in this section achieves more than sufficient performance and is preferably used.

The remaining components on the measurement system are responsible for signal processing, signal transmission and to provide all required auxiliary supply voltages for the components. Furthermore, there are two optical connections, which act as trigger input and output to synchronize the system with other isolated measurement systems or even to synchronize with an oscilloscope using the (external) trigger input/output. As seen in Fig. 5(b), the finalized measurement system is realized very compact with overall dimensions of 95 mm × 32 mm × 30 mm including the rechargeable battery (indicated with a dashed box; accounts for roughly 1/3 of the total volume), which allows an operating time >2 hours (power consumption between 1.5 W and 2 W).

C. LOW COUPLING CAPACITANCE ISOLATED POWER SUPPLY UNIT

Battery-operated measurement systems have the advantage that no additional power supply connections and/or isolation capacitances towards PE are required, which by increasing the with careful design achieved small C_{earth}, potentially degrade the CMRR. A fundamental drawback, however, is their limited operating time before manual intervention in the measurement setup is required to recharge or replace the battery. A compact overall solution (small C_{earth}) is only possible with relatively low capacity batteries, hence there is an inherent trade-off between operating time and system size. To achieve unlimited measurement time, a low coupling
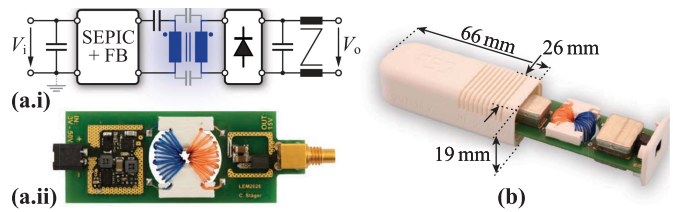
FIGURE 7. (a.i) Block diagram of the developed wide input voltage range (5 – 50 V) 5 W output power isolated auxiliary PSU composed of a Single-Ended Primary Inductance Converter (SEPIC) plus series resonance operated full-bridge transformer driver, featuring an isolation stage (1 : 1 transformer) with very low coupling capacitance (highlighted in blue). Pictures of the PSU (b) without and (c) with metallic shields, plastic enclosure and overall dimensions.

capacitance isolated PSU is therefore required. Power-over-Fiber (PoF) solutions with highly compact photovoltaic cells illuminated by a laser beam can transmit several Watts of electrical power over wide distances with virtually unlimited isolation [30], [31]. PoF is used in different applications such as commercially available isolated probes [6], [7], [8] or as isolated GD PSU [32], [33]. Such solutions are, however, relatively large, expensive and show a poor conversion efficiency (overall electrical-to-optical-to-electrical efficiency <5 % for an electrical output power of 1.5 W [34], [35]). Due to the poor efficiency, the resulting relatively high heat generation demands an increased cooling effort. An alternative solution is a custom-designed galvanically isolated PSU with magnetic isolation using a carefully constructed transformer with low coupling capacitance C_c. Thereby, a significantly higher conversion efficiency and a much more compact design is possible. Fig. 7(a.i) and (a.ii) show the block diagram and the PCB of the PSU with a wide input voltage range of $V_i = 5$ V ... 50 V to allow versatile connection to different power sources. It is designed to deliver up to 5 W output power (enough to simultaneously charge the battery and operate the measurement system plus sufficient margin). The input stage is composed of a single-ended primary inductance converter (SEPIC) followed by a Full-Bridge (FB) transformer driver. The total coupling capacitance C_c of the isolation transformer is composed of a contribution from primary winding to core (N49 material from TDK) and from core to secondary winding (series connection of two times winding-to-core capacitance C_{w-c}, assuming an electrically conductive core at HF in the multi-MHz range [36]), and of a contribution directly from primary to secondary winding (15 turns each) over the air (winding-to-winding capacitance C_{w-w}). With the winding placement as indicated in Fig. 7(a.ii), i.e., a large separation between primary and secondary winding, C_c is mainly defined by the winding-to-core capacitance C_{w-c}. To minimize C_{w-c}, the primary and secondary windings are placed several mm away from the magnetic core to finally achieve a total coupling capacitance of $C_c \approx 2$ pF. The placement is realized with a 3D printed plastic shell of several mm thickness, in which the core is placed before the windings are added. Placement of the windings as described comes at the expense of
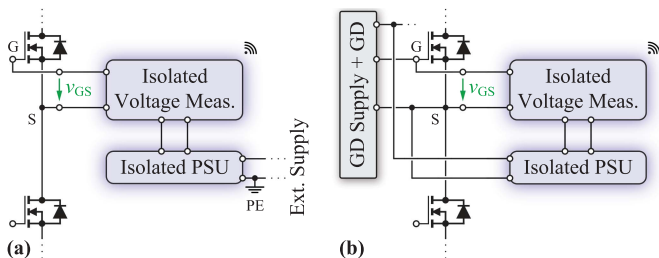
659

FIGURE 8. Different options to connect the isolated auxiliary PSU to the isolated voltage measurement system. (a) Ground (PE) referenced auxiliary PSU input (e.g., laboratory supply). (b) Connection directly to a floating auxiliary power source on the DUT itself (e.g., GD supply referred to the high-side switch source potential).

an increased leakage inductance L_σ and therefore, a reduced coupling factor, which is compensated by operating the FB transformer driver in series resonance (resonance capacitor indicated in Fig. 7(a.i)) in order to avoid a load dependent output voltage. The output stage is unregulated and consists of a diode rectifier and an output filter. All required supply voltages are generated directly on the measurement system with regulated point-of-load converters from the unregulated PSU output voltage (≈ 14 V). Fig. 7(b) shows the fully assembled PSU with mounted shields and a plastic enclosure that has an overall conversion efficiency above 70 %. The purpose of the metallic shields is on the one hand to prevent disturbing nearby equipment (e.g., GDs) with the emissions from the switch-mode operation of the SEPIC and transformer driver and on the other hand, conversely, to prevent distortions of the PSU in a noisy/harsh environment found, e.g., in close vicinity to fast switching power converters. The power connection between PSU output and measurement system is realized with a coaxial cable equipped with lossy ferrite cores acting as additional decoupling CM inductors. Like in the tip cable, this helps to decouple the additional C_{earth} of the PSU output stage from the fast switching transitions. In contrast to the virtually unlimited isolation of PoF solutions, the isolation capabilities of the measurement system and therefore, the maximum allowed CM input voltage range is now defined by the transformer isolation, assuming the primary side is referred to PE, e.g., connected to a non-isolated external laboratory supply as shown in Fig. 8(a). The isolation is verified up to 1 kV, which is sufficient for many applications. Transformers for isolated GD supplies with an isolation rating of 10 kV and at the same time extremely compact construction and very low coupling capacitance have been presented [37] and could be used in this auxiliary PSU. However, thanks to the wide input voltage range, it is possible to power the auxiliary PSU directly from a floating source, e.g., from an auxiliary GD supply in a MV power converter as shown in Fig. 8(b), where the additional power consumption of around 2–3 W is negligible [38]. Thereby, the transformer isolation only has to withstand the voltage difference between measurement reference potential and PSU input voltage reference potential and the rating of 1 kV is sufficient. The PSU has no significant impact on the
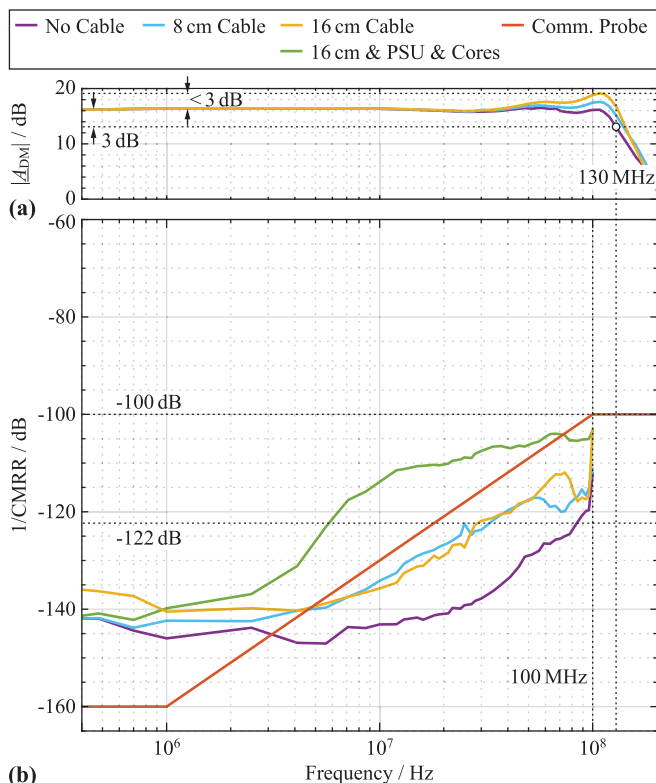

FIGURE 9. (a) Measured DM TFs of the probe without tip cable (purple), with a 8 cm tip cable (cyan) and with a 16 cm tip cable (yellow), achieving in all cases a BW > 130 MHz and < 3 dB peaking. (b) Measured CMRR for battery operation with the same configurations as (a). For easier comparison with Fig. 3, 1/CMRR curves (negative dB values) are plotted. The green line shows 1/CMRR for the long tip cable with PSU operation. Further indicated is 1/CMRR of the currently best available commercial isolated voltage probe (orange).

achievable CMRR, as experimentally verified in the next section.

IV. EXPERIMENTAL VERIFICATION

This section presents measurement results in the frequency- and the time-domain to experimentally verify the performance of the designed isolated measurement system.

A. FREQUENCY-DOMAIN CHARACTERIZATION

The analog BW is determined by measuring the magnitude $|\underline{A}_{\text{DM}}|$ of the DM TF, depicted in Fig. 9(a). Thereby, the AFE is configured for maximum sensitivity, i.e., set to the highest gain of 16 dB ($\times 6.3$) and no input voltage divider is utilized. The measurement has been performed without tip cable (purple) and with 8 cm (cyan) and 16 cm (yellow) long tip cables. As indicated, the -3 dB BW is 130 MHz in the case without tip cable. The BW is intentionally limited by the AAF in order to prevent aliasing effects in the sampling process. With the current sampling rate of 400 MSPS, the Nyquist frequency and therefore, the absolute maximum possible BW, is 200 MHz, whereas the corner frequency of 130 MHz is selected to account for finite filter steepness. To overcome the BW limitation imposed by the ADC, faster

sampling devices would be required. A certain peaking in the magnitude response is visible proportional to the tip cable length. It originates from a resonance between the leakage inductance of L_{CM} (cf. Fig. 6(a)), the additional inductance and capacitance from the tip cable and the AFE input capacitance. With the 16 cm long cable (nominal configuration offering high flexibility to connect to different DUTs), the peaking is below 3 dB. In the current realization, the tip cable is purely capacitive and inductive, i.e., does not contain any distributed damping. Peaking could be reduced by utilizing a lossy transmission line, as it is done in standard passive voltage probes [39], instead of a nearly perfect conducting copper coaxial cable. In addition, a better frequency response and in particular a lower input capacitance could then be achieved by placing R_1 and C_1 of the voltage divider directly at the measurement tip. Thereby, the cable capacitance is in parallel to C_2 and does not add to the input capacitance seen by the DUT (less loading).

Fig. 9(b) shows 1/CMRR (i.e., negative dB values to directly compare with Fig. 3) versus frequency, again for the different configurations, where in case of utilized tip cables, CM cores are distributed along the full cable length (cf. i) above). These measurements are performed in a carefully defined environment, where the measurement system is placed on an isolated distance holder inside a shielded box (referred to PE) with a distance of $\approx$15 cm to the walls. The input pins at the measurement tip are shorted together and excited with a 160 V peak-to-peak sinusoidal CM voltage (with respect to PE) at distinct frequencies up to 100 MHz using a power amplifier (AR 150A100D with maximum frequency of 100 MHz). The measured error is evaluated in the digital domain and to maximize the measurement sensitivity, the system's AFE is configured for maximum gain such that referred to the input, one Least Significant Bit (LSB) of the ADC corresponds to 0.13 mV. Therefore, the maximum directly measurable CMRR is 122 dB (one LSB toggles due to the CM excitation). CMRR values >122 dB are obtained by averaging the amplitude extracted over multiple recorded signal periods (>1000 periods per frequency). This takes into account that the LSB does not toggle every time, indicating a lower error voltage than the equivalent of one LSB. The best results (CMRR >120 dB across almost the full considered frequency range) are achieved by connecting the measurement system without tip cable (purple) because Z_{line} is accordingly minimized and the full i_{CM} flows entirely over the shielding enclosure. Adding a tip cable with CM cores (cyan for 8 cm length, yellow for 16 cm length), the CMRR decreases by around 10 dB in the frequency range between 10 MHz and 100 MHz. The cable length does not significantly influence the performance up to 70 MHz. For the nominal configuration with the 16 cm long tip cable equipped with CM cores, the green curve shows the impact of using the isolated PSU instead of the battery. There, the CMRR decrease compared to the same configuration with battery operation is between 10 and 25 dB, starting at a few MHz. It can be seen that for all configurations of the presented measurement system, the
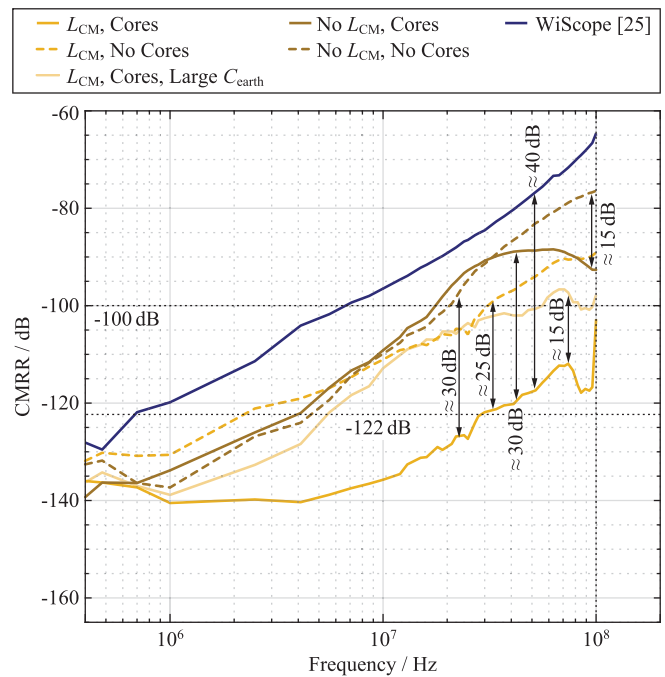

FIGURE 10. Influence of different measures listed in Section III-B on the achievable CMRR (16 cm long tip cable attached in all cases) and comparison with the WiScope [25]. For easier comparison with Fig. 3, 1/CMRR is plotted.

CMRR is substantially greater than 100 dB over the full considered frequency range and on par with the best-performing currently available isolated voltage probe (orange).

Moreover, Fig. 10 demonstrates the influence of the different measures (cf. Section III-B) on the achievable CMRR (y-axis again showing 1/CMRR, i.e., negative dB values, for easier comparison with Fig. 3), where in all cases the 16 cm long tip cable is attached to the measurement system. The yellow curves denote configurations with mounted internal CM choke L_{CM} (cf. Fig. 6(a)), which show $\approx$30 dB better HF performance compared to the configurations with L_{CM} unmounted (brown curves). In case of installed L_{CM}, the tip cable equipped with CM cores (continuous yellow line) gives a benefit of $\approx$25 dB compared to a tip cable without CM cores (dashed yellow line). For an absent L_{CM} the benefit is smaller, and only at frequencies above 30 MHz a maximum improvement of $\approx$15 dB is measured. Between the best-performing configuration (yellow continuous line, all measures from Section III-B employed) and worst-performing configuration (brown dashed line, no cable CM cores, no L_{CM}), a difference of $\approx$30–35 dB is found. An important finding for practical use is that a larger C_{earth}, formed, e.g., by placing the measurement system too close to PE, only degrades the CMRR by $\approx$15 dB (semi-transparent yellow line). This proves the effectiveness of the provided measures to decouple i_{CM} from the sensitive measurement path. A comparison of the presented system's CMRR with the WiScope [25] reveals an improvement of $\approx$ 40 dB over a very wide frequency range. The WiScope CMRR (darkblue curve in Fig. 10) is thereby measured without any
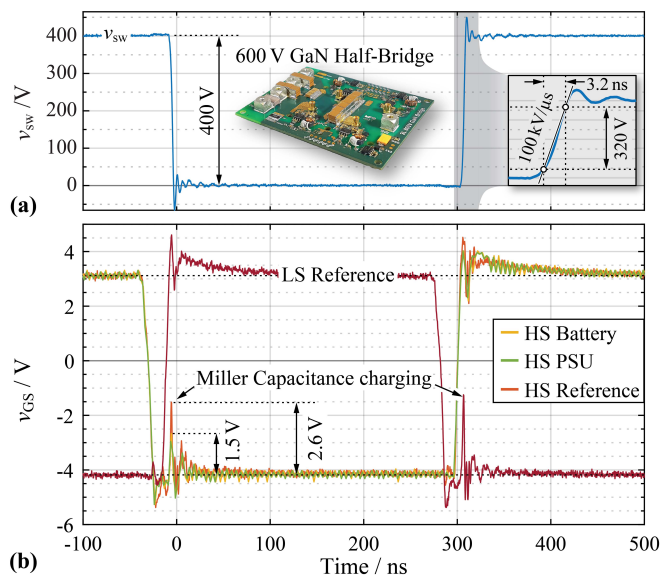
FIGURE 11. Measurement of the HS Gate-Source voltage in a GaN half-bridge (cf. Fig. 1(a)) with 400 V dc link voltage. (a) Measured switch-node voltage, i.e., CM disturbance voltage, with a dv/dt of 100 kV/μs. (b) Measured $v_{\mathrm{GS,HS}}$ with the commercial isolated probe (orange; HS reference measurement) and the presented system with the 16 cm triaxial tip cable and CM cores on the cable with battery operation (yellow) and PSU operation (green). For further reference, the LS Gate-Source voltage is measured (red; LS reference measurement) to prove that the residual peak in v_{GS} during the fast voltage transition is due to the current that flows out of the gate to charge the device Miller capacitance.

tip cable, i.e., marks the absolute best-case, whereas the presented measurement system is equipped with the 16 cm long tip cable. Based on Fig. 9(b), with the addition of a tip cable the WiScope's HF CMRR is expected to degrade by >10 dB.

B. TIME-DOMAIN MEASUREMENTS
Finally, the measurement system is tested by measuring the HS GS voltage $v_{\mathrm{GS,HS}}$ in a half-bridge employing 600 V GaN power semiconductors (cf. Fig. 1(a)), switching $V_{\mathrm{dc}} = 400$ V at 800 kHz. Fig. 11(a) shows the measured switch-node waveform v_{sw} for Zero-Current Switching (ZCS), i.e., without any load and/or output filter connected. A zoomed view into the rising edge indicates a very fast dv/dt of 100 kV/μs. The measured $v_{\mathrm{GS,HS}}$ is depicted in Fig. 11(b) where again, the results of the presented measurement system operated with the battery (yellow) and the PSU (green) are compared to the best available commercial isolated voltage probe (orange). In all cases, the 16 cm long triaxial tip cable equipped with CM cores is used. The proposed measurement system accurately captures $v_{\mathrm{GS,HS}}$, however, the BW of 130 MHz is just at the lower limit for measurements of signals with a rise time of only few nanoseconds. During the falling edge of v_{sw}, where $v_{\mathrm{GS,HS}}$ is supposed to be steady at -4 V to safely keep the HS switch off, a certain voltage peak occurs. This peak is measured with all probes/system configurations, however, seems to be worse when measured with the reference probe (2.6 V compared to 1.5 V). To determine, whether the peak is an error due to the CM disturbance or indeed present, in addition, the
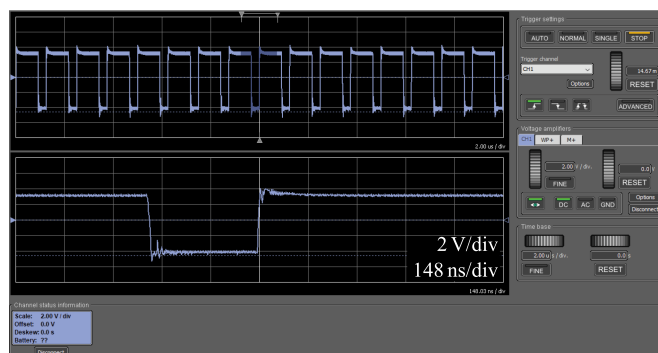

FIGURE 12. Screenshot of the Graphical User Interface (GUI) software on the host computer displaying the $v_{\mathrm{GS,HS}}$ measurement when the probe is battery-operated (yellow curve in Fig. 11(b)).

LS GS voltage $v_{\mathrm{GS,LS}}$ is measured with the reference probe (dark red). The peak is present in the same way as in the $v_{\mathrm{GS,HS}}$ measurement and is a result of Miller capacitance C_{GD} (between gate and drain) charging during the falling edge of v_{sw}. This current has to flow out of the GD and causes the voltage peak. Therefore, the presented isolated measurement system as well as the reference probe are not influenced by the fast changing CM voltage. However, the supposedly smaller $v_{\mathrm{GS,HS}}$ peak measured with the presented system during the v_{sw} transition is due to the lower BW compared to the reference probe. Fig. 12 shows a screenshot of the GUI on the host computer, displaying the $v_{\mathrm{GS,HS}}$ measurement of the battery-operated configuration (corresponding to the yellow curve in Fig. 11(b)).

V. CONCLUSION
Very fast switching transitions (high dv/dt) achieved with today's increasingly prevalent Wide-Bandgap (WBG) semiconductors in power converters require advanced measurement technologies to accurately investigate the dynamic behavior during operation. The demands on the measurement technology are particularly high, since often measurements of small voltages referred to rapidly changing reference potentials that act as Common Mode (CM) disturbance on the measurement, must be carried out. A prominent example is the measurement of the High-Side (HS) Gate-Source (GS) voltage in a half-bridge, where the switch-node voltage acts as CM disturbance. Such situations demand equipment with superior Common Mode Rejection Ratio (CMRR) to avoid affecting the desired measurement. Switching transitions of multiple 100 V within sub 10 ns lead to significant High-Frequency (HF) disturbances, thus a high CMRR at elevated frequencies is necessary. The minimum required CMRR over the full frequency range of interest is determined to constrain the resulting time-domain error in the measured signal below a certain limit $\Delta v_{\varepsilon,\mathrm{pp}}$. This value is found to be constant ($\Delta v_{\varepsilon,\mathrm{pp}}/V_{\mathrm{dc}}$) up to a frequency f_{c2}, determined solely by the transition time of the CM disturbance ($f_{\mathrm{c2}} = \mathrm{d}v/\mathrm{d}t/(\pi V_{\mathrm{dc}})$) and above there, rises with $+20$ dB/dec. Therefore, for given V_{dc}, dv/dt and maximum allowed measurement error, the

required CMRR versus frequency is directly obtainable and is independent of the converter switching frequency f_{sw}. For $V_{dc} = 800\,V$ and $dv/dt = 100\,kV/\mu s$, a CMRR of around $80\,dB$ up to $40\,MHz$ is required to keep the resulting error below $100\,mV$. There are commercially available galvanically isolated voltage measurement *probes* that achieve the demanded CMRR. However, they require a dedicated (often vendor-specific) oscilloscope to form a complete measurement system. As an alternative, this work presents a galvanically isolated measurement *system*, which digitizes the measured signal and transmits the data wireless to a host device (e.g., computer, laptop, tablet) with corresponding host Graphical User Interface (GUI) software, to directly and independent of other equipment perform measurements on fast changing reference potentials. Essential design aspects, in particular of the Analog Front-End (AFE) and the connection of the measurement system to a Device Under Test (DUT), imperative to achieve a HF CMRR >100 dB at frequencies in the multi-MHz range, are highlighted and thoroughly analyzed.

Finally, the presented isolated measurement system is comprehensively tested in the frequency- and the time-domain. It achieves a measurement Bandwidth (BW) of 130 MHz and a CMRR of >100 dB up to 100 MHz, which is on par with the best commercially available isolated voltage probes. Time-domain measurements of the HS GS voltage in a half-bridge with fast-switching Gallium Nitride (GaN) power semiconductors verify the superior CM robustness but indicate that for capturing very fast switching transients, a higher measurement BW is required. Currently, the BW is ultimately limited by the sampling rate of the Analog-to-Digital Converter (ADC) but this could be overcome with a faster sampling device. Moreover, optical trigger synchronization with other measurement equipment is an important next implementation step to increase practical usability.

REFERENCES

[1] D. Cittanti, E. Vico, and I. R. Bojoi, "New fom-based performance evaluation of 600/650 V SiC and GaN semiconductors for next-generation EV drives," *IEEE Access*, vol. 10, pp. 51693–51707, 2022.

[2] J. A. Anderson, G. Zulauf, J. W. Kolar, and G. Deboy, "New figure-of-merit combining semiconductor and multi-level converter properties," *IEEE Open J. Power Electron.*, vol. 1, pp. 322–338, 2020.

[3] S. Biswas, D. Reusch, M. de Rooij, and T. Neville, "Evaluation of measurement techniques for high-speed GaN transistors," in *Proc. 5th Workshop Wide Bandgap Power Devices Appl.*, Albuquerque, NM, USA, 2017, pp. 105–110.

[4] J. Böhler et al., "Ultra-high-bandwidth power amplifiers: A technology overview and future prospects," *IEEE Access*, vol. 10, pp. 54613–54633, 2022.

[5] I. Lee and X. Yao, "Active voltage balancing of series connected sic MOSFET submodules using pulsewidth modulation," *IEEE Open J. Power Electron.*, vol. 2, pp. 43–55, 2021.

[6] "Isolated measurement systems - TIVH," Tektronix, Inc. 2017, Accessed : Jul. 20th, 2022, [Online]. Available: https://download.tek.com/datasheet/TIVH-Series-IsoVu-Measurement-Systems-Datasheet-51W612172.pdf

[7] "Isolated measurement systems - TIVP," Tektronix, Inc. 2020, Accessed: Jul. 20th, 2022. [Online]. Available: https://download.tek.com/datasheet/TIVP-Datasheet-51W616553.pdf

[8] "Dl-ISO high voltage optically isolated probe," Teledyne LeCroy, Inc. 2022, Accessed: Jul. 20th, 2022. [Online]. Available: https://cdn.teledynelecroy.com/files/pdf/dl-iso-probe-datasheet.pdf

[9] "HVFO103 high-voltage fiber optically isolated probe," Teledyne LeCroy, Inc. 2019, Accessed: Jul. 20th, 2022, [Online]. Available: https://cdn.teledynelecroy.com/files/manuals/high-voltage-fiber-optic-probe-operators-manual.pdf

[10] "HVFO108 high voltage fiber optically-isolated probe," Teledyne LeCroy, Inc. 2020, Accessed: Jul. 20th, 2022. [Online]. Available: https://cdn.teledynelecroy.com/files/pdf/hvfo-probes-datasheet.pdf

[11] "Fiber optic isolated voltage probe. ISOVP," Saker Tech S.L., 2020, Accessed : Jul. 20th, 2022. [Online]. Available: https://saker-mv.com/wp-content/uploads/2020/06/ISOVP-Fiber-Isolated-Voltage-Probe.pdf

[12] "CS448 isolated channel oscilloscope specification," Cleverscope Ltd., 2019, Accessed: Jul. 20th, 2022. [Online]. Available: https://www.cleverscope.com/files/CS448%20Specification.pdf

[13] "CS548 isolated channel oscilloscope specification," Cleverscope Ltd., 2022, Accessed: Jul. 20th, 2022. [Online]. Available: https://cleverscope.com/files/CS548%20Specification%20v1.0.pdf

[14] Y. Qiu, J. Vanderkloot, R. Hou, and J. Lu, "Diagnosing for cross-conduction in GaN half-bridge," in *Proc. Appl. Power Electron. Conf. Expo.*, New Orleans, LA, USA, 2020, pp. 2577–2583.

[15] A. Nara, "A measurement of the gate-emitter voltage waveform of IGBT in a motor driver circuit," in *Proc. IEEE Instrum. Meas. Technol. Conf.*, Hamamatsu, Japan, 1994, vol. 2, pp. 623–626.

[16] P. S. Niklaus, D. Bortis, and J. W. Kolar, "Next generation measurement systems with high common-mode rejection," in *Proc. 19th IEEE Workshop Control Model. Power Electron.*, Padua, Italy, 2018, pp. 1–8.

[17] H. Geramirad, F. Morel, B. Lefebvre, C. Vollaire, and A. Breard, "Measuring small differential-mode voltages with high common-mode voltages and fast transients–application to gate drivers for wide bandgap switches," in *Proc. Int. Symp. Electromagn. Compat.*, Rome, Italy, 2020, pp. 1–5.

[18] T. Funaki and K. Hayashi, "Estimation of residual common mode voltage in floating voltage measurement with differential voltage probe for high voltage power electroincs circuit," in *Proc. CPMT Symp. Jpn.*, Kyoto, Japan, 2018, pp. 91–94.

[19] D. Rothmund, D. Bortis, and J. W. Kolar, "Accurate transient calorimetric measurement of soft-switching losses of 10-kV SiC MOSFETs and diodes," *IEEE Trans. Power Electron.*, vol. 33, no. 6, pp. 5240–5250, 2018.

[20] R. Hebner, R. Malewski, and E. Cassidy, "Optical methods of electrical measurement at high voltage levels," *Proc. IEEE*, vol. 65, no. 11, pp. 1524–1548, Jun. 1977.

[21] C. A. Bleys, "Floating input, optically isolated, high-voltage measurement probe," *Rev. Sci. Instrum.*, vol. 47, no. 5, pp. 621–623, 1976.

[22] W. H. Siew, Y. C. Liu, B. Musa, F. Mir, and Y. Wang, "Basis for a wireless network for EMC measurements in electric substations," in *Proc. IEEE Int. Symp. Electromagn. Compat.*, Honolulu, HI, USA, 2007, pp. 1–5.

[23] G. Crotti, D. Gallo, D. Giordano, C. Landi, and M. Luiso, "Medium voltage divider coupled with an analog optical transmission system," *IEEE Trans. Instrum. Meas.*, vol. 63, no. 10, pp. 2349–2357, Oct. 2014.

[24] W. Siew, Y. Wang, and M. Faheem, "Digital wireless electromagnetic interference (EMI) data acquisition system," in *Proc. Int. Symp. Electromagn. Compat.*, Chicago, IL, USA, 2005, vol. 2, pp. 342–345.

[25] Y. Lobsiger, G. Ortiz, D. Bortis, and J. W. Kolar, "Concept and experimental evaluation of a novel DC- 100 MHz wireless oscilloscope," in *Proc. Int. Power Electron. Conf.*, Hiroshima, Japan, 2014, pp. 1309–1316.

[26] F. Costa and D. Magnon, "Graphical analysis of the spectra of EMI sources in power electronics," *IEEE Trans. Power Electron.*, vol. 20, no. 6, pp. 1491–1498, Nov. 2005.

[27] B. Schroeder, "How the heck do i measure a gate drive slewing at 70 kV/us?," in *Proc. Power Convers. Intell. Motion Conf.*, Nuremberg, Germany, 2017, pp. 1–7.

[28] M. J. Mende, G. W. Reed, J. D. Pileggi, K. A. Rinder, R. A. Booman, and M. V. Pelt, "Flexible resistive tip cable assembly for differential probing," U. S. Patent10,302,676 B2, May 2019.

[29] R. Pallas-Areny and J. Webster, "Common mode rejection ratio in differential amplifiers," *IEEE Trans. Instrum. Meas.*, vol. 40, no. 4, pp. 669–676, Aug. 1991.

[30] J.-G. Werthen, "Powering next generation networks by laser light over fiber," in *Proc. Opt. Fiber Commun. Conf./Nat. Fiber Opt. Eng. Conf.*, San Diego, CA, USA, 2008, Art. no. OWO3.

[31] M. Matsuura, H. Nomoto, H. Mamiya, T. Higuchi, D. Masson, and S. Fafard, "Over 40-W electric power and optical data transmission using an optical fiber," *IEEE Trans. Power Electron.*, vol. 36, no. 4, pp. 4532–4539, Apr. 2021.

[32] X. Zhang et al., "A gate drive with power over fiber-based isolated power supply and comprehensive protection functions for 15-kV SiC MOSFET," *IEEE Trans. Emerg. Sel. Topics Power Electron.*, vol. 4, no. 3, pp. 946–955, Sep. 2016.

[33] S. Heinig, K. Jacobs, S. Norrga, and H.-P. Nee, "Single-fiber combined optical power and data transmission for high-voltage applications," in *Proc. 46th IEEE Annu. Ind. Electron. Soc. Conf.*, Singapore, 2020, pp. 1473–1480.

[34] "PPM-010C MIH laser source," MH GoPower, 2021, Accessed : Jul. 21, 2022. [Online]. Available: http://www.mhgopower.com/images/PPM-010C_Datasheet_Rev_1.6_10-01-2021.pdf

[35] "YCH-h003 MIH photovoltaic power converter," MH GoPower, 2022, Accessed: Jul. 21st, 2022. [Online]. Available: http://www.mhgopower.com/images/YCH-H003_15V_PPC_Datasheet_Rev_2.0_04-29-2022.pdf

[36] F. Fiorillo, C. Beatrice, O. Bottauscio, and E. Carmi, "Eddy-current losses in MN-ZN ferrites," *IEEE Trans. Magn.*, vol. 50, no. 1, Jan. 2014, Art. no. 6300109.

[37] D. Rothmund, D. Bortis, and J. W. Kolar, "Highly compact isolated gate driver with ultrafast overcurrent protection for 10 kV SiC MOSFETs," *CPSS Trans. Power Electron. Appl.*, vol. 3, no. 4, pp. 278–291, 2018.

[38] J. Stewart, J. Motwani, J. Yu, I. Cvetkovic, and R. Burgos, "Improved power density of a 6 kV, 1 mW power electronics building block through insulation coordination," in *Proc. 23rd IEEE Workshop Control Model. Power Electron.*, Tel Aviv, Israel, 2022, pp. 1–7.

[39] J. R. Kobbe and W. J. Polits, "Electrical probe," U. S. Patent 2,883,619, Apr. 1959.

PASCAL S. NIKLAUS (Student Member, IEEE) received the B.Sc. and M.Sc. degrees (with distinction) in electrical engineering from the Swiss Federal Institute of Technology (ETH) Zurich, Zurich, Switzerland, in 2016 and 2018, respectively. During studies he did two internships where he developed hardware, firmware and software for custom and off-the-shelf test and measurement equipment with Duagon AG, Dietikon, Switzerland, and working on the firmware development for a new microprocessor architecture with ACP AG, Zurich, Switzerland. In April 2018 he joined the Power Electronic Systems Laboratory (PES) at ETH Zurich, as a Doctoral Student focusing on advanced measurement technologies in the field of power electronics and on high bandwidth power converters featuring wide-bandgap power semiconductors.

RETO BONETTI received the B.Sc. and M.Sc. degrees in electrical engineering and information technology from the Swiss Federal Institute of Technology (ETH) in Zurich, Zurich, Switzerland, in 2018 and 2020, respectively. In August 2020, he joined the Power Electronics Systems Laboratory (PES) at ETH Zurich, as a Ph.D. student, where he is working on active magnetic bearings featuring large air gaps with integrated wireless power transfer. His research interests include power electronics, electrical drive systems, and control theory.

CHRISTOF STÄGER received the B.Sc. and M.Sc. degree in electical engineering and information technology from the Swiss Federal Institute of Technology (ETH) Zurich, Zurich, Switzerland, in 2020 and 2022, respectively. During the master's studies he was a Hardware Design Engineer with the Laboratory for High Power Electronic Systems, ETH Zurich.

JOHANN W. KOLAR (Fellow, IEEE) received the M.Sc. and Ph.D. degree (*summa cum laude*) from the University of Technology Vienna, Vienna, Austria, in 1997 and 1999, respectively. Since 1984, he has been an independent Researcher and International Consultant with close collaboration with the Vienna University of Technology, Vienna, Austria, in the fields of power electronics, industrial electronics and high performance drive systems. He was appointed Assoc. Professor and Head 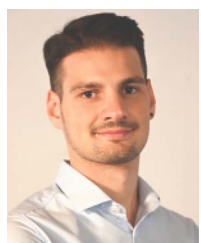of the Power Electronic Systems Laboratory with the Swiss Federal Institute of Technology (ETH) Zurich, Zurich, Switzerland, on Feb. 1, 2001, and was promoted to the rank of Full Prof. in 2004. Dr. Kolar has proposed numerous novel converter concepts incl. the Vienna Rectifier, Sparse Matrix Converter and the Swiss Rectifier, has spearheaded the development of x-million rpm motors, and has pioneered fully automated multi-objective power electronics design procedures. He has Graduated more than 80 Ph.D. students, has authored or coauthored more than 1000 journal and conference papers and four book chapters, and has filed more than 200 patents. He has presented more than 30 educational seminars at leading international conferences and has served as IEEE PELS Distinguished Lecturer from 2012 to 2016. He was the recipient of more than 40 IEEE Transactions and Conference Prize Paper awards, 2014 IEEE Power Electronics Society R. David Middlebrook Achievement Award, 2016 IEEE PEMC Council Award, 2016 IEEE William E. Newell Power Electronics Award, 2021 EPE Outstanding Achievement Award and two ETH Zurich Golden Owl awards for excellence in teaching. He is the Fellow of the IEEE and was elected to the U.S. National Academy of Engineering as an international member in 2021. His research interests include ultra-compact/efficient WBG converter systems, ANN-based design procedures, solid-state transformers, ultra-high speed drives, bearingless motors, and life cycle analysis of power electronics converter systems.

DOMINIK BORTIS (Senior Member, IEEE) received the M.Sc. and Ph.D. degrees in electrical engineering from the Swiss Federal Institute of Technology (ETH) Zurich, Zurich, Switzerland, in 2005 and 2008, respectively. In May 2005, he joined the Power Electronic Systems Laboratory (PES), ETH Zurich, as a Ph.D. Student. From 2008 to 2011, he was the Postdoctoral Fellow and from 2011 to 2016 Research Associate with PES. Since January 2016, he has been heading the Research Group Advanced Mechatronic Systems with PES, which concentrates on ultra-high speed motors, bearingless drives, linear-rotary actuator and machine concepts with integrated power electronics. He has authored or coauthored more than 90 scientific papers in international journals and conference proceedings and has filed more than 30 patents. His research interests include highly dynamic positioning systems, medical systems, and future mobility concepts. He was the recipient of ten IEEE Conference Prize Paper Awards and two First Prize Transaction Paper Awards.